IET Power Electronics

Research Article

IET Journals
The Institution of Engineering and Technology

Novel modified phase-shift modulation strategy for isolated AC–DC power converters

ISSN 1755-4535
Received on 1st August 2019
Revised 3rd November 2019
Accepted on 10th December 2019
E-First on 14th January 2020
doi: 10.1049/iet-pel.2019.0895
www.ietdl.org

Marcelo Llomplat[1] ✉, Jonathan E. Bosso[1], Roberto E. Carballo[2], Guillermo O. García[1]

[1]Grupo de Electrónica Aplicada (GEA) – Instituto de Investigaciones en Tecnologías Energéticas y Materiales Avanzados (IITEMA) – CONICET, Facultad de Ingeniería, Universidad Nacional de Río Cuarto Ruta Nacional 36, km 601, Río Cuarto, Córdoba, Argentina

[2]Instituto de Materiales de Misiones (IMAM) – Grupo de Investigación y Desarrollo en Ingeniería Electrónica (GID-IE) – CONICET, Facultad de Ingeniería – Universidad Nacional de Misiones, Juan Manuel de Rosas 325, Oberá, Misiones, Argentina

✉ *E-mail: marcelollomplat@gmail.com*

Abstract: Different power converter topologies are used to perform the energy exchange between an AC grid and a DC source belonging to a hybrid electric micro-grid. A single-phase single-stage isolated AC–DC power converter is one of them. Moreover, this power converter can operate under different modulation strategies. The phase-shift modulation (PSM) strategy is capable of varying the phase between the voltages applied to the high-frequency transformer terminals of the power converter in order to control the energy flow in both directions. Based on the PSM strategy, this study presents a novel modified PSM strategy capable of controlling the power flow in both directions and obtaining a current with low total harmonic distortion and a power factor close to 1 for the entire operating range on the AC side. Considering the novel modulation strategy to be proposed, a comparison of three PSM-based modulation strategies was carried out taking into account the total harmonic distortion of current injected into the AC grid, the power factor and the average power transferred. A theoretical analysis was carried out and the results obtained were validated by means of experimental results.

1 Introduction

Electricity demand and electric energy generation through renewable energy sources such as wind, photovoltaic, hydraulic and so on are ever-growing. In this context, it is necessary to integrate the renewable energy sources with the conventional electric power system through power electronic converters which allow to control more efficiently the electric energy in terms of generation, distribution, transmission, consumption and storage [1].

Electricity generation distributed through renewable resources is a key factor for modern society, but its integration with the conventional electric power system presents great challenges in terms of energy quality [2].

A network which can integrate different energy sources and loads through a DC bus, an AC bus or a combination of both is called a micro-grid. The advantages and disadvantages of the micro-grid with a DC bus and an AC bus are presented in [3, 4].

A micro-grid can be interconnected with the conventional electric power system or not. This type of interconnection can be carried out by means of a DC–AC isolated bidirectional power electronic converter.

In the literature analysed, different types of converter topologies were found based on the operating principle of dual active bridge (DAB) converters [5] which can increase or decrease voltage levels and perform DC–DC energy conversion in an isolated and bidirectional way.

Based on the operating principle of the DAB converter, the power exchange between an AC grid and a DC bus can be achieved through different conversion stages [6].

In [7], the DC–AC conversion requires an intermediate stage of conversion DC–DC which uses an additional DC bus with its capacitors, respectively. These capacitors can be large and expensive [8]. Otherwise, there are different topologies that perform DC–AC conversion in an isolated and bidirectional way without the need for an intermediate stage of conversion [9–15].

These types of isolated and bidirectional DC–AC converters are commonly used in topologies called solid-state transformers (SST) [16, 17].

Fig. 1 shows the schematic diagram of the single-phase single-stage isolated DC–AC converter.

Different modulation strategies are used to control the power flow. The modulation strategies to be mentioned below can be applied for DC–DC and DC–AC topologies taking into account the voltage amplitude on the AC side is variable in a grid period for a DC–AC converter.

The phase-shift modulation (PSM) strategy controls the power transfer bidirectionally by changing the phase between the voltages applied to the power converter's high-frequency transformer terminals. In [5, 18], this strategy is applied to DC–DC and DC–AC converters, respectively.

In [19], a combination of the trapezoidal modulation (TZM) and triangular modulation (TRM) strategies to reduce power losses in a given operating range for a DC–DC converter is presented. These strategies operate the DC–DC converter in order to make the waveform of the current through the high-frequency transformer trapezoidal or triangular.

Based on PSM, TZM and TRM strategies, a hybrid modulation strategy applied to a DC–DC converter for ultracapacitor applications to extend the control range to lower power levels is proposed in [20].

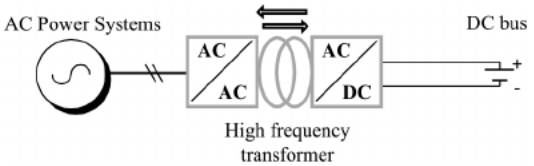

Fig. 1 *Schematic diagram of the single-phase single-stage isolated DC–AC power converter*

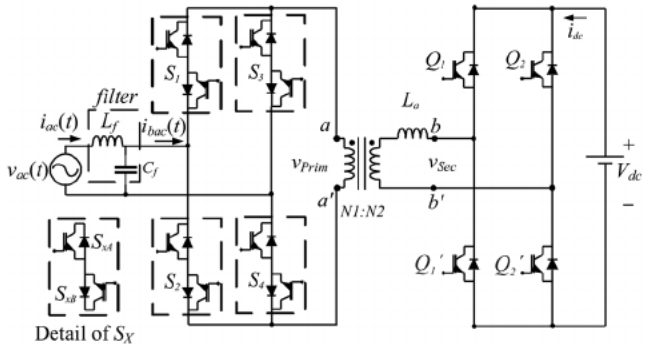

Fig. 2 *Topology of the single-phase single-stage DC–AC power converter*

Table 1 Switching states

AC H-bridge $v_{ac}(t) > 0$			AC H-bridge $v_{ac}(t) < 0$			DC H-bridge		Voltages	
S_{1A}			S_{1B}						
S_{2B}	S_{1B}	S_{2A}	S_{2A}	S_{2B}	S_{1A}	Q_1	Q_2	v_{Prim}	v_{Sec}
S_{3B}	S_{4B}	S_{3A}	S_{3A}	S_{3B}	S_{4A}				
S_{4A}			S_{4B}						
1	1	0	1	1	0	1	0	$+v_{ac}$	$+V_{dc}$
1	0	1	1	0	1	0	1	$-v_{ac}$	$-V_{dc}$
1	1	0	1	1	0	0	0	$+v_{ac}$	0
1	0	1	1	0	1	1	1	$-v_{ac}$	0

In [21], a new modulation scheme for a DC–DC converter is presented. This scheme allows selection of a specific mode of operation to generate the minimum RMS current on the inductor which produces minimal copper and conduction losses.

To increase the efficiency over a wide range of the DC–DC converter operation, the PSM, TZM and TRM modulation strategies are combined in [22].

In [23], a dual-phase-shift modulation strategy is proposed to eliminate reactive power in the DC–DC converter and in [24] a detailed characterisation of the DC–DC converter is performed using this modulation strategy.

The implementation and transition between the different modulation strategies applied to the DC–DC converter are relatively complicated. Therefore, in [25], a simple and flexible concept for generating pulse width modulation signals for all possible modulation strategies is presented.

The modulation strategy introduced in [10] controls the single-phase DC–AC converter under soft switching for the operating range in internal mode and achieves a current with low total harmonic distortion (THD*i*) and power factor (PF) close to 1 on the AC side.

A combined phase-shift and frequency modulation is applied in an isolated and bidirectional single-phase DC–AC converter in order to obtain a current with low THD*i* and PF close to 1 on the AC side. This process is carried out under a soft-switching operation range [12].

In order to extend the soft-switching operation range within a certain range of power transferred, a sinusoidal pulse width modulation is used to obtain a current in the AC side with PF close to 1 and lower THD*i* [15].

The operation point where the maximum value of transferred power is obtained occurs when the modulated voltages applied to the high-frequency transformer terminals of the power converter reach a 50% duty cycle and a 90° phase angle between them [5, 18, 26].

The above-mentioned papers for the single-phase single-stage isolated AC–DC converter do not evaluate the converter at the maximum power transfer operating point because the total harmonic distortion of the current is increased.

Considering the maximum power transfer operating point, three modulation strategies based on PSM are introduced in this paper.

The novel modified phase-shift modulation (mPSM) strategy proposed in this paper allows controlling the power transferred and obtain a PF close to 1 and an AC current with lower harmonic distortion (THD*i*) for entire operation range of the isolated single-phase single-stage DC–AC converter.

A topology description and a theoretical analysis of the operation principle of the single-phase single-stage bidirectional isolated DC–AC converter are presented in Section 2 of this paper. Considering the modulation strategy to be proposed, a mathematical analysis of the three PSM-based modulation strategies is presented in Section 3. The experimental results confirming theoretical predictions and the method of AC filter design are presented in Section 4. Lastly, conclusions are presented in Section 5.

2 Topology description and operating principle

This section presents a single-phase single-stage DC–AC power converter used to interconnect a conventional single-phase AC grid with a DC source represented by a DC bus belonging to a hybrid electric micro-grid. In this paper, the voltage of the DC bus called V_{dc} is considered constant in a switching period and the voltage of the single-phase AC grid can be represented by

$$v_{ac}(t) = V_{ac}\sin(\omega_r t) \tag{1}$$

where V_{ac} is the maximum value of the AC voltage, $\omega_r = 2\pi f_r = 2\pi/T_r$, f_r is the grid frequency in Hz and T_r is the grid period in seconds.

The power converter used in [10] allows to increase or decrease the voltage levels, control the power flow in a bidirectional way and isolate the single-phase AC grid with the DC bus through a high-frequency transformer. The topology of the single-phase single-stage DC–AC power converter is shown in Fig. 2.

This converter is composed of two H-bridges and a high-frequency transformer which, together with an auxiliary inductance L_a, are used as an interface to interconnect the DC and AC sides.

The DC H-bridge is implemented via unidirectional switches with their corresponding anti-parallel diodes which are responsible for imposing the modulated voltage v_{Sec} between the terminals of b and b'. The AC H-bridge is implemented via voltage and current bidirectional switches, with their corresponding anti-parallel diodes. The former are responsible for imposing the modulated voltage v_{Prim} between terminals a and a'.

The transformation ratio is defined as $n = N2/N1$, where $N1$ and $N2$ represent the number of winding turns on the AC side and DC side, respectively.

In order to mitigate the harmonic components produced in the AC grid current $i_{ac}(t)$ by the commutations in the power devices, a low-pass filter must be used [27]. The AC filter design method will be explained afterwards taking the transferred power and the system parameters into account.

The converter operation principle is based on power flow control by means of phase-shift applied between the modulated voltage v_{Sec} and v_{Prim}. In this paper, the phase shift is represented by δ.

In the AC H-bridge, each bidirectional switch is implemented with two unidirectional switches which are represented as S_{xA} and its complementary S_{xB}. The DC H-bridge switches are represented as Q_x, where x corresponds to the switch number.

The power devices of each leg of the DC H-bridge are switched in a complementary way and, with the aim of avoiding overvoltages in the switches of the AC H-bridge, the following switching states are established as shown in Table 1 [28].

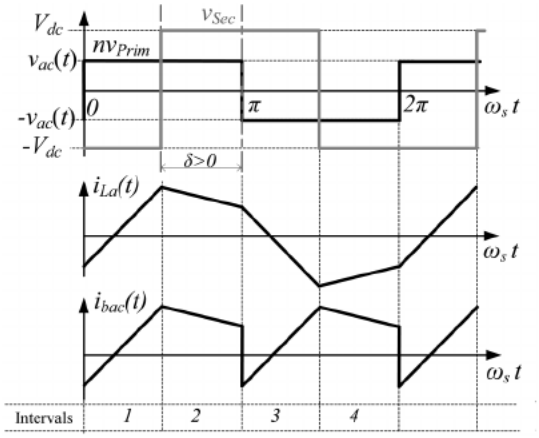

Fig. 3 *Waveform in a switching period of nv_{Prim} and v_{Sec} voltages, and $i_{La}(t)$ and $i_{bac}(t)$ currents for $\delta > 0$*

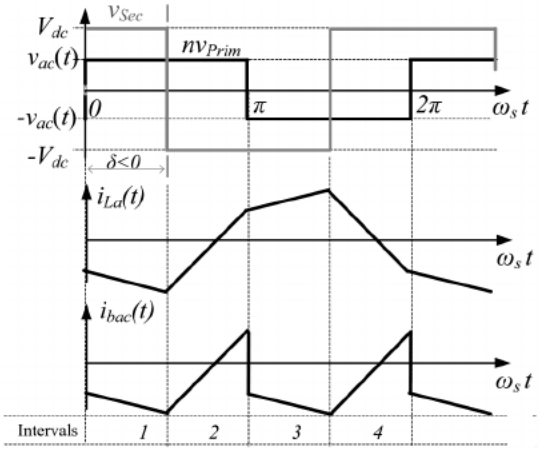

Fig. 4 *Waveform in a switching period of nv_{Prim} and v_{Sec} voltages, and $i_{La}(t)$ and $i_{bac}(t)$ currents for $\delta < 0$*

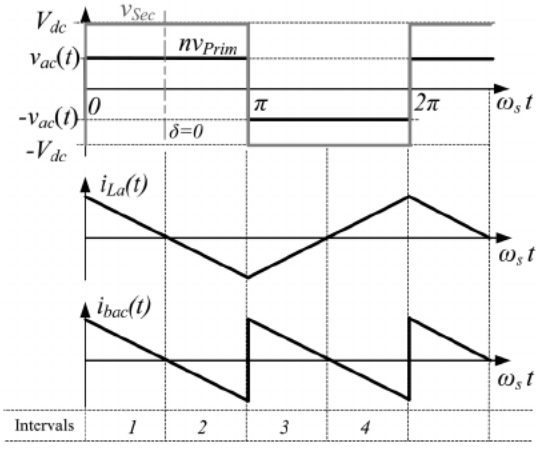

Fig. 5 *Waveform in a switching period of nv_{Prim} and v_{Sec} voltages, and $i_{La}(t)$ and $i_{bac}(t)$ currents for $\delta = 0$*

3 Modulation strategy

This section presents a modulation strategy, which consists in switching the power devices of both H-bridges in order to impose a voltage v_{Prim} between the terminals a and a' and another v_{Sec} between the terminals b and b' with a duty cycle of 50% and constant frequency.

The AC H-bridge switches are activated with a certain phase shift δ with respect to the DC H-bridge switches. Furthermore, the average power transfer and the current waveform of the AC grid can be adjusted according to the variation of phase shift as will eventually be explained.

Power devices are switched with an angular frequency defined as

$$\omega_s t = 2\pi f_s = 2\pi/T_s \tag{2}$$

where f_s is the switching frequency in Hz, and T_s is the switching period in second.

Three cases can be mentioned in relation to the power flow transferred between the AC side and the DC side. The first case corresponds to $\delta > 0$ where the power transfer is made from the AC side to DC side; the second case for $\delta < 0$ where the power transfer is made from the DC side to the AC side, and, finally, for $\delta = 0$, the power transfer is zero.

Figs. 3–5 show the waveforms in a switching period of the voltages nv_{Prim} and v_{Sec}, the instantaneous current through L_a and the instantaneous current at the AC H-bridge input, defined in this paper as $i_{La}(t)$ and $i_{bac}(t)$, respectively, for the three cases considered.

On the other hand, the converter behaviour can be deduced from a mathematical model based on the waveform of the instantaneous current through L_a.

To find the expression of the instantaneous current in L_a, the intervals 1 ($0 < \omega_s t < \delta$) and 2 ($\delta < \omega_s t < \pi$) are established and δ is measured with respect to nv_{Prim} considering the centres of each of the nv_{Prim} and v_{Sec} modulated voltages.

Equations of instantaneous current for each interval are defined by

$$\begin{aligned} i_{La1}(t) &= \frac{1}{\omega_s L_a}\int_0^{\delta} V_{La}\, d\omega_s t \\ &= \frac{(nv_{\text{Prim}} - v_{\text{Sec}})}{L_a \omega_s}\omega_s t + i_{La}(0) \end{aligned} \tag{3}$$

$$\begin{aligned} i_{La2}(t) &= \frac{1}{\omega_s L_a}\int_{\delta}^{\pi} V_{La}\, d\omega_s t \\ &= \frac{(nv_{\text{Prim}} - v_{\text{Sec}})}{L_a \omega_s}(\omega_s t - \delta) + i_{La}(\delta) \end{aligned} \tag{4}$$

where V_{La} is the voltage applied to terminals of L_a, $i_{La1}(t)$ and $i_{La2}(t)$ are the equations of the instantaneous currents applied in L_a for intervals 1 and 2, respectively, and $i_{La}(0)$ and $i_{La}(\delta)$ are the initial currents applied in L_a for intervals 1 and 2, respectively.

The initial currents values can be obtained by

$$\begin{aligned} i_{La}(0) = &-\frac{(nv_{\text{Prim}} - v_{\text{Sec}})}{2L_a \omega_s}(\pi - \delta) \\ &-\frac{(nv_{\text{Prim}} + v_{\text{Sec}})}{2L_a \omega_s}(\delta) \end{aligned} \tag{5}$$

$$i_{La}(\delta) = -\frac{(nv_{\text{Prim}} - v_{\text{Sec}})}{2L_a\omega_s}(\pi - \delta) + \frac{(nv_{\text{Prim}} + v_{\text{Sec}})}{2L_a\omega_s}(\delta) \tag{6}$$

In addition, $i_{bac}(t)$ current is a reflection of $i_{La}(t)$ current affected by the transformation ratio n and inverted by the switching sequence established. Therefore, in the intervals corresponding to 1-2 and 3-4, $i_{bac}(t)$ current presents the same waveform as can be observed in Figs. 3–5.

The average value of $i_{bac}(t)$ in a switching period can be deduced from

$$\begin{aligned} i_{\text{acSw}} &= n\frac{1}{\pi}\int_0^{\pi} i_{bac}(t)\,\mathrm{d}\omega_s t \\ &= n\frac{1}{\pi}\left(\int_0^{\pi} i_{La1}(t)\,\mathrm{d}\omega_s t + \int_0^{\pi} i_{La2}(t)\,\mathrm{d}\omega_s t\right) \\ &= n\frac{V_{\text{dc}}}{L_a\pi\omega_s}\delta(\pi - \delta) \end{aligned} \tag{7}$$

In (7), the value of i_{acSw} during each commutation period depends on the system parameters and is a function of the variable δ. Therefore, it can be deduced that the current waveform during a grid period can be controlled by means of δ variation during different time intervals as shown in Fig. 6.

In this paper, the phase variation with time is defined as a mPSM.

On the other hand, the waveform of $i_{\text{ac}}(t)$ current and the waveform of synthesised i_{acSw} current in a grid period can be considered the same.

With the aims of performing a theoretical analysis of the waveform of $i_{\text{ac}}(t)$ in a grid period using different mPSM strategies to operate the power converter, (7) can be rewritten as shown in (8) when taking into account the following considerations: $nV_{\text{dc}}/(L_a\pi\omega_s) = 1, f_1(t) = \delta(t)\pi$ and $f_2(t) = \delta(t)^2$.

$$i_{\text{ac}}t = f_1(t) - f_2(t) \tag{8}$$

For positive or negative $\delta(t)$ values, the term of $f_2(t) = \delta(t)^2$ is always positive. To resolve this issue, the $f_2(t)$ function can be written as $f_2(t) = \text{sign}(\delta(t))\delta(t)^2$ where $\text{sign}(\delta(t)) = \delta(t)/|\delta(t)|$.

Additionally, the following equations are used to evaluate the total harmonic distortion of the $i_{\text{ac}}(t)$ current (THDi) and the PF [29]

$$\text{THD}i = \frac{\sqrt{i_{\text{ac(rms)}}^2 - i_1^2}}{i_1} \tag{9}$$

$$\text{PF} = \frac{1}{\sqrt{1 + \text{THD}i^2}}\text{DPF} \tag{10}$$

where i_{ac}(rms) is the effective value of current $i_{\text{ac}}(t)$ and i_1 its fundamental component. DPF is the displacement power factor.

For the first mPSM proposed to operate the power converter, a triangular function is used as defined in the following equation:

$$\delta_1(t, k) = k\arcsin(\sin(\omega_s t)) \tag{11}$$

where $\delta_1(t, k)$ is the first mPSM, which corresponds to a triangular function, and $|k| \leq 1$ is a constant proportional to the peak value of the signal.

The power converter operation with $\delta_1(t, k)$ and $k = 1$ produces the waveforms of $f_1(t)$, $f_2(t)$ and $i_{\text{ac}}(t)$ with their corresponding frequency spectrum as shown in Fig. 7.

Regarding the theoretical analysis of the waveform of $i_{\text{ac}}(t)$ in Fig. 7, it can be deduced that the difference between $f_1(t)$ and $f_2(t)$ results in current $i_{\text{ac}}(t)$ which is satisfied by (8), both in time and frequency domains.

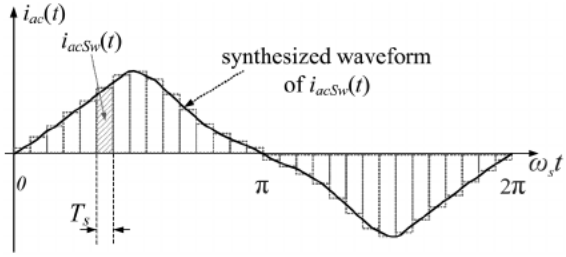

Fig. 6 *Waveform of synthesised current i_{acSw} in a grid period*

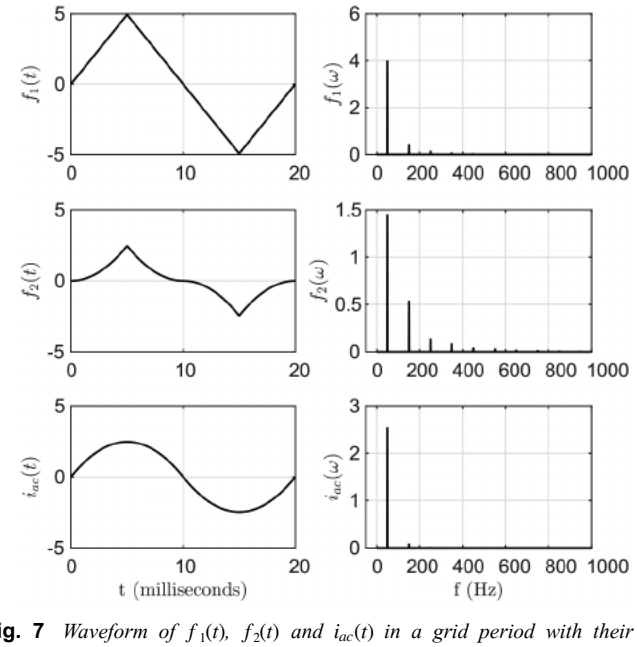

Fig. 7 *Waveform of $f_1(t)$, $f_2(t)$ and $i_{ac}(t)$ in a grid period with their corresponding frequency spectrum using modulation $\delta_1(t, k)$ with $k = 1$*

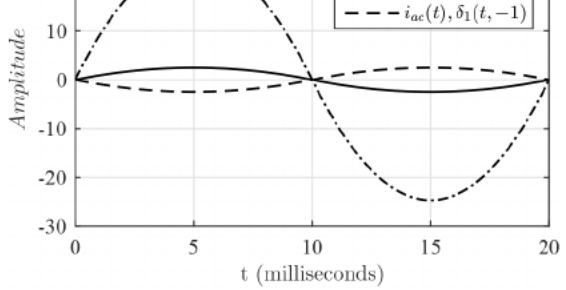

Fig. 8 *Waveform of $v_{ac}(t)$ and $i_{ac}(t)$ in a grid period using $\delta_1(t, k)$ with $k = 1$ and $k = -1$*

The PF value reached is close to 1 across the entire operating range.

In order to verify bidirectional power flow, the waveforms $v_{\text{ac}}(t)$ and $i_{\text{ac}}(t)$ in a grid period while the converter is being operated with values $\delta_1(t, k) > 0$ with $k = 1$ and $\delta_1(t, k) < 0$ with $k = -1$, respectively, are shown in Fig. 8.

On the other hand, the operation of the power converter with $\delta_1(t, k)$ for values of $|k| < 1$ results in two particular cases defined by the intervals between $0.7 < |k| < 1$ for the first case and $|k| < 0.7$ for the second case.

In the first interval, the decrease of the third harmonic component in $i_{\text{ac}}(t)$ produces lower THDi percentages than the THDi percentage obtained for $k = 1$.

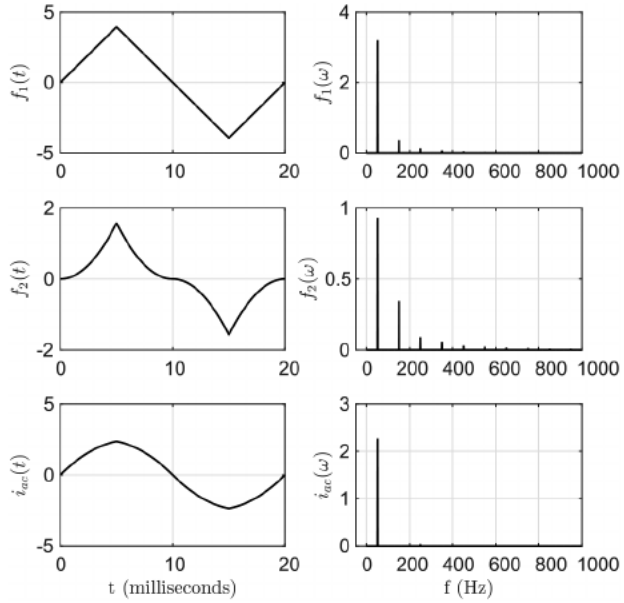

Fig. 9 *Waveform of $f_1(t)$, $f_2(t)$ and $i_{ac}(t)$ in a grid period with their corresponding frequency spectrum using modulation $\delta_1(t,k)$ with $k = 0.8$*

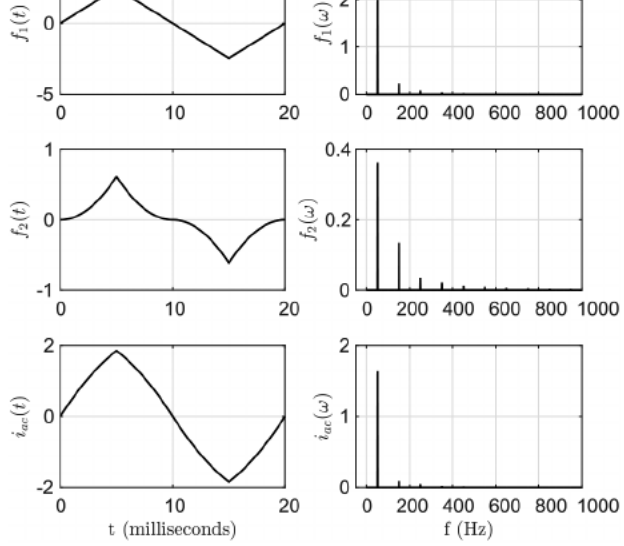

Fig. 10 *Waveform of $f_1(t)$, $f_2(t)$ and $i_{ac}(t)$ in a grid period with their corresponding frequency spectrum using modulation $\delta_1(t,k)$ with $k = 0.5$*

By contrast, in the second interval, the odd harmonic components of $i_{ac}(t)$ which increase the THDi percentage to a higher value than for $k = 1$ are more preponderant.

The theoretical analysis of $i_{ac}(t)$ for both cases can be deduced from (8) in both time and frequency domains.

In addition, the resulting waveforms of $f_1(t)$, $f_2(t)$ and $i_{ac}(t)$ obtained with their corresponding frequency spectrum for $k = 0.8$ and $k = 0.5$ are shown in Figs. 9 and 10, respectively.

The THDi percentages achieved are close to 2.1 and 6.21% for $k = 0.8$ and $k = 0.5$, respectively, while the PF values obtained across the entire operating range are close to 1.

For the second mPSM strategy proposed to operate the power converter, a sinusoidal function is used as defined in the following equation:

$$\delta_2(t,k) = k(\pi/2)\sin(\omega_r t) \tag{12}$$

where k is a constant proportional to the peak value of signal $\delta_2(t,k)$.

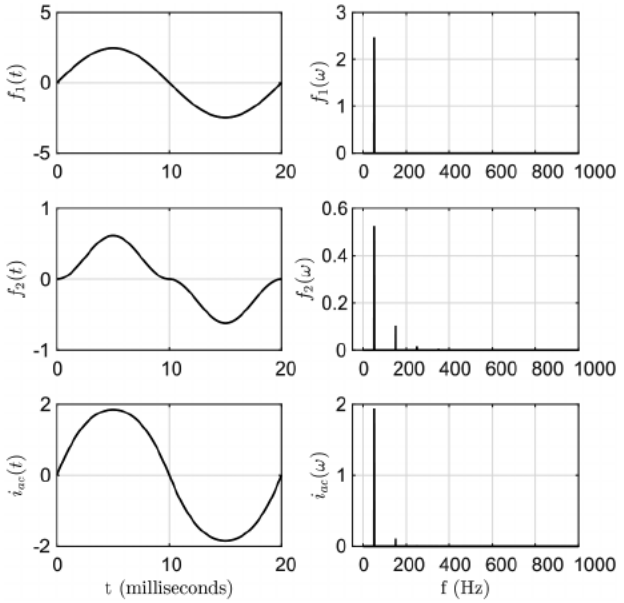

Fig. 11 *Waveform of $f_1(t)$, $f_2(t)$ and $i_{ac}(t)$ in a grid period with their corresponding frequency spectrum using modulation $\delta_2(t,k)$ with $k = 0.5$*

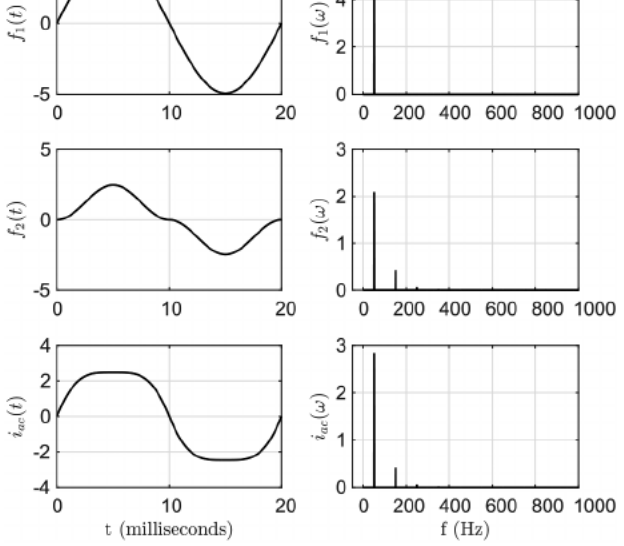

Fig. 12 *Waveform of $f_1(t)$, $f_2(t)$ and $i_{ac}(t)$ in a grid period with their corresponding frequency spectrum using modulation $\delta_2(t,k)$ with $k = 1$*

Similar to the analysis performed when the converter is operated with $\delta_1(t,k)$, it can be deduced that when the amplitude of $f_1(t)$ is greater than amplitude of $f_2(t)$, the difference between both increases and, therefore, the waveform of $i_{ac}(t)$ approximates a sinusoidal function of frequency $\omega_r$as shown in Fig. 11.

By contrast, when the difference between the amplitudes of $f_1(t)$ and $f_2(t)$ decreases, the waveform of $i_{ac}(t)$ no longer approximates a sinusoidal function, which increases the THDi value as shown in Fig. 12.

In addition, the analysis performed for both cases is satisfied by (8) in both time and frequency domains.

The calculated percentage of THDi is close to 5.44% for $k = 0.5$ and 14.91% for $k = 1$. The PF values obtained across the entire operating range are close to 1.

With the objectives of controlling the average power value transferred and obtaining a sinusoidal waveform of $i_{ac}(t)$ with the lowest total harmonic distortion and a PF close to 1 for the entire operating range, the novel mPSM strategy is developed below.

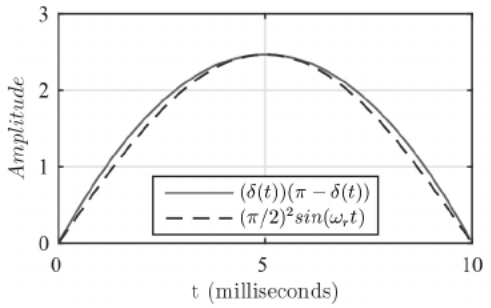

Fig. 13 *Waveform of current in a half grid period produced by the values obtained from $i_{ac}(t)$ during each switching period using the mPSM strategy $\delta_1(t,k)$ with $k=1$*

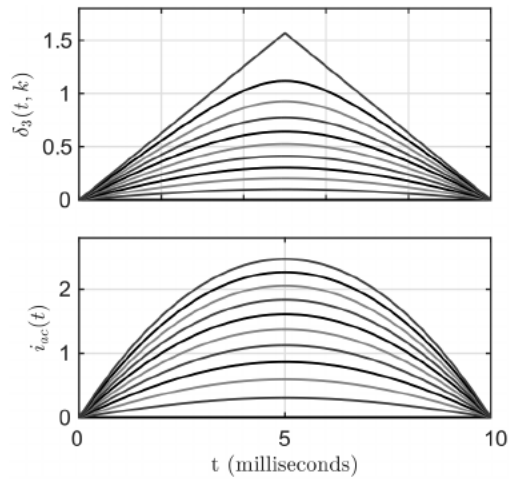

Fig. 14 *Waveform of $\delta_3(t,k)$ and $i_{ac}(t)$ in a half grid period considering $V_{dc}/L_e\pi\omega_s=1$ and with intervals of k equal to 0.1*

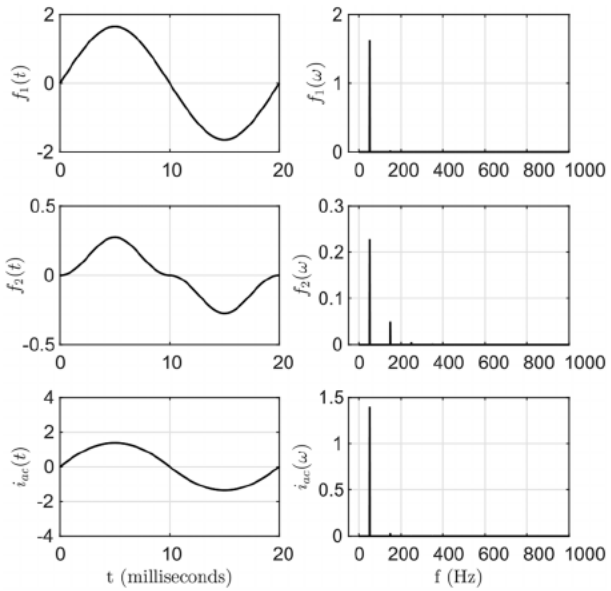

Fig. 15 *Waveform of $f_1(t)$, $f_2(t)$ and $i_{ac}(t)$ in a grid period with their corresponding frequency spectrum using modulation $\delta_3(t,k)$ with $k=0.5$*

Similar to the analysis conducted in [18], an approximately sinusoidal waveform is achieved when the power converter operates with $\delta_1(t,k)$ and $k=1$.

A comparison of the $i_{ac}(t)$ waveform obtained for $\delta_1(t,k)$ and $k=1$ with a sinusoidal function defined as $(\pi/2)^2\sin(\omega_r t)$ is shown in Fig. 13.

The previous approximation can be considered as

$$i_{ac}(t)=\delta_1(t,k)(\pi-\delta_1(t,k))\simeq(\pi/2)^2\sin(\omega_r t) \tag{13}$$

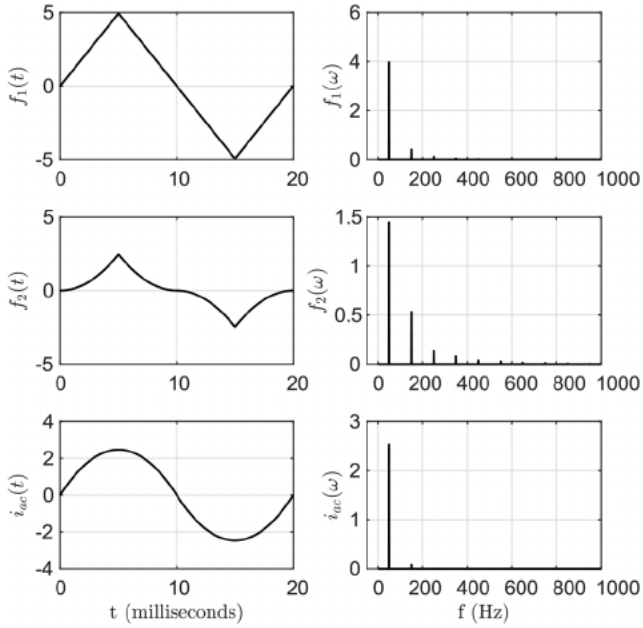

Fig. 16 *Waveform of $f_1(t)$, $f_2(t)$ and $i_{ac}(t)$ in a grid period with their corresponding frequency spectrum using modulation $\delta_3(t,k)$ with $k=1$*

Additionally, the function $\omega_r t$ in (13) can be replaced by the mPSM strategy defined in this work as a $\delta_3(t,k)$, which results in

$$i_{ac}(t)\simeq(\pi/2)^2\sin(\delta_3(t,k)) \tag{14}$$

With the aim of achieving a $i_{ac}(t)$ current whose waveform approximates a sinusoidal function of frequency ω_r for the entire operating range, (15) is proposed. The previous one imposes as a condition that the waveform of $i_{ac}(t)$ has to be always equal to a sinusoidal function defined as $k'\sin(\omega_r t)$ for the entire operating range

$$i_{ac}(t)=k'\sin(\omega_r t) \tag{15}$$

To obtain an mPSM strategy $\delta_3(t,k)0$, the second terms of both equations in (14) and (15) can be matched to solve $\delta_3(t,k)$ as indicated in the following equation:

$$\begin{aligned}&(\pi/2)^2\sin(\delta_3(t,k))=k'\sin(\omega_r t)\\&\delta_3(t,k)=\arcsin\left(k'\frac{4}{\pi^2}\sin(\omega_r t)\right)\end{aligned} \tag{16}$$

Finally, with the aim of normalising the obtained mPSM strategy $\delta_3(t,k)$ as a function of k, (16) can be rewritten considering $k<0$ as $\left|k'(4/\pi^2)\right|\leq 1$ as shown in the following equation:

$$\delta_3(t,k)=\arcsin(k\sin(\omega_r t)) \tag{17}$$

In order to evaluate the obtained mPSM strategy $\delta_3(t,k)$, the power converter is operated using different intervals of k defined every 0.1.

Fig. 14 shows the waveforms of $\delta_3(t,k)$ and $i_{ac}(t)$ in a half grid period obtained during the operation of the power converter with $0<k\leq 1$.

Otherwise, the waveforms of $\delta_3(t,k)$ and $i_{ac}(t)$ obtained for $-1\leq k<0$ are the same as in Fig. 14 but with negative polarity.

In Figs. 15 and 16, the waveforms of $f_1(t)$, $f_2(t)$ and $i_{ac}(t)$ are shown in a grid period with their corresponding frequency spectrum when the power converter is operated with $\delta_3(t,k)$ for $k=0.5$ and $k=1$, respectively.

Similarly to the analysis performed by the mPSM strategies $\delta_1(t,k)$ and $\delta_2(t,k)$, the theoretical analysis of $i_{ac}(t)$ when the power

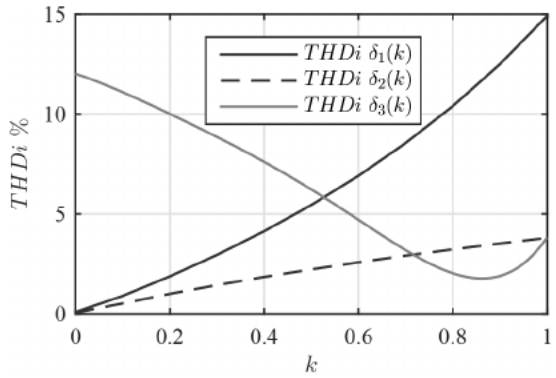

Fig. 17 *Theoretical results of THDi% as a function of the factor k for each mPSM strategy used*

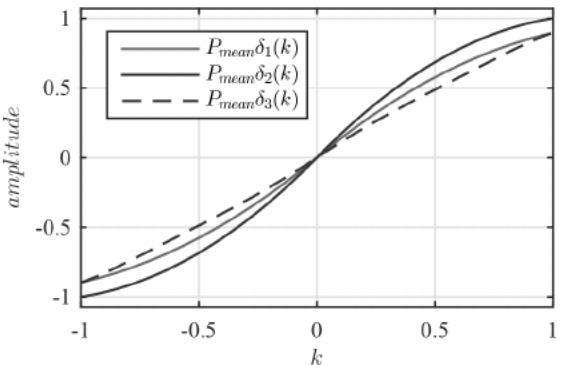

Fig. 18 *Theoretical results of the normalised average power $P_{mean}\delta_1(k)$, $P_{mean}\delta_2(k)$ and $P_{mean}\delta_3(k)$ as a function of k*

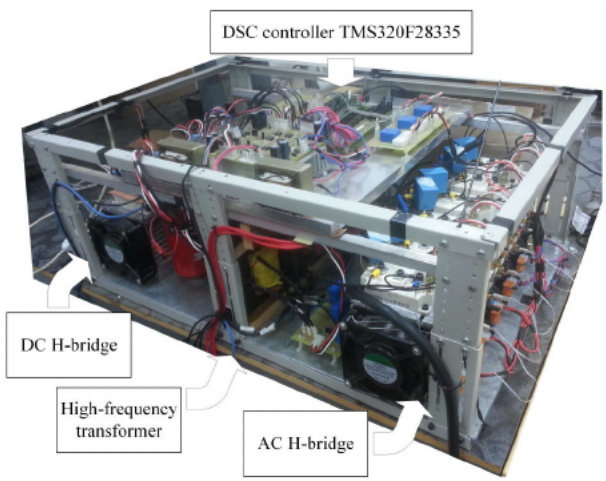

Fig. 19 *Laboratory prototype*

Table 2 System parameters

V_{ac}	V_{dc}	f_r	f_s	n	L_a
311 V	311 V	50 Hz	20 kHz	0.6	475 μH

converter is operated with the mPSM strategy $\delta_3(t,k)$ can be performed and satisfied by (8) both in time and frequency domains.

The THDi values obtained are close to 2.22% for $k = 0.5$ and 3.8% for $k = 1$. The PF values obtained across the entire operating range are close to 1.

Consequently, the mPSM strategy $\delta_3(t,k)$ allows to operate the power converter obtaining an $i_{ac}(t)$ current whose waveform approximates a sinusoidal wave of grid frequency. PF close to 1 and THDi percentage lower than 5% are obtained for the entire operating range.

With the objective of evaluating the average power transferred for each mPSM strategy used, the following analysis can be performed.

With the aim of evaluating the total harmonic distortion of current $i_{ac}(t)$ across the entire operation range for the three modulation strategies presented, the theoretical curves of the THDi percentage as a function of the factor k are displayed in Fig. 17.

3.1 Calculation of the average power transferred

The theoretical average power transferred can be determined by

$$P_{\text{mean}} = \frac{1}{\pi}\int_{\pi}^{0}\left(\frac{1}{\pi}\int_{\pi}^{0} V_{\text{Prim}} i_{La}(t)\,\mathrm{d}\omega_s t\right)\mathrm{d}\omega_r t \tag{18}$$

By solving (18) for each of the proposed mPSM strategies, the following equations can be obtained:

$$P_{\text{mean}}\delta_1(k) = \frac{nV_{\text{ac}}V_{\text{dc}}}{L_a\pi^2\omega_s}k(2\pi + 4k - 2\pi k) \tag{19}$$

$$P_{\text{mean}}\delta_2(k) = \frac{nV_{\text{ac}}V_{\text{dc}}}{12L_a\omega_s}k(3\pi - 4k) \tag{20}$$

$$P_{\text{mean}}\delta_3(k) = \frac{nV_{\text{ac}}V_{\text{dc}}}{L_a 2\pi^4\omega_s}((\pi+\pi^4)\arcsin(k) - (1+\pi^3)\arcsin^2(k)) \tag{21}$$

where $P_{\text{mean}}\delta_1(k)$, $P_{\text{mean}}\delta_2(k)$ and $P_{\text{mean}}\delta_3(k)$ are the equations of the average power for each of the modulation strategies $\delta_1(t,k)$, $\delta_2(t,k)$ and $\delta_3(t,k)$, respectively.

Fig. 18 shows the normalised average power values per unit for the entire converter operating range using each of the mPSM strategies.

To evaluate the average power transfer achieved by each of the mPSM strategies used, in Fig. 18, it can be deduced that the maximum power transferred by mPSM $\delta_2(t,k)$ strategy is greater than the maximum power $P_{\text{mean}}\delta_1(k)$ and $P_{\text{mean}}\delta_3(k)$ by <10%.

By operating the power converter with mPSM strategies $\delta_1(t,k)$ and $\delta_3(t,k)$, the maximum power reached is the same.

4 Experimental results

In order to validate the proposed mPSM strategies, the experimental results were obtained through a laboratory prototype which operates with single-phase or three-phase power systems. The laboratory prototype is shown in Fig. 19.

The experimental results were obtained by means of a laboratory prototype built to operate up to three-phase grid, as shown in Fig. 19.

The auxiliary inductance and the high-frequency transformer were built with ferrite core and litz wire to reduce power loses.

In AC H-bridge and DC H-bridge, the SEMIKRON power devices used are SKM150GM12T4G and SKM150GB12T4G, respectively.

A digital Texas Instrument DSC controller TMS320F28335 was implemented to run the modulation algorithms.

To compare the experimental results with the previous mathematical analysis, the system parameters were chosen taking into account that $V_{\text{dc}}/(L_a\pi\omega_s) \simeq 1$ as shown in Table 2.

With the aim of mitigating the harmonic components in the $i_{\text{ac}}(t)$ current, the low-pass filter was designed taking into account the power transferred and the system parameters.

In order to build the prototype, the low-pass filter detailed in Section 4.1 and the parameters indicated in Table 2 were taken into consideration.

On the other hand, the experimental results obtained below were achieved with the objective of evaluating the three mPSM strategies presented for the operation range $|k| \leq 1$.

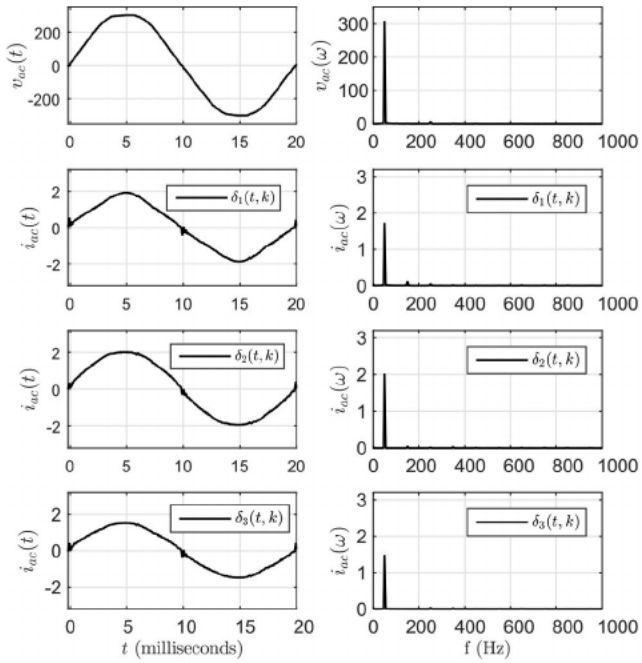

Fig. 20 *Experimental results of $v_{ac}(t)$ and $i_{ac}(t)$ in a grid period using the modulations $\delta_1(t,k)$, $\delta_2(t,k)$ and $\delta_3(t,k)$ with $k = 0.5$*

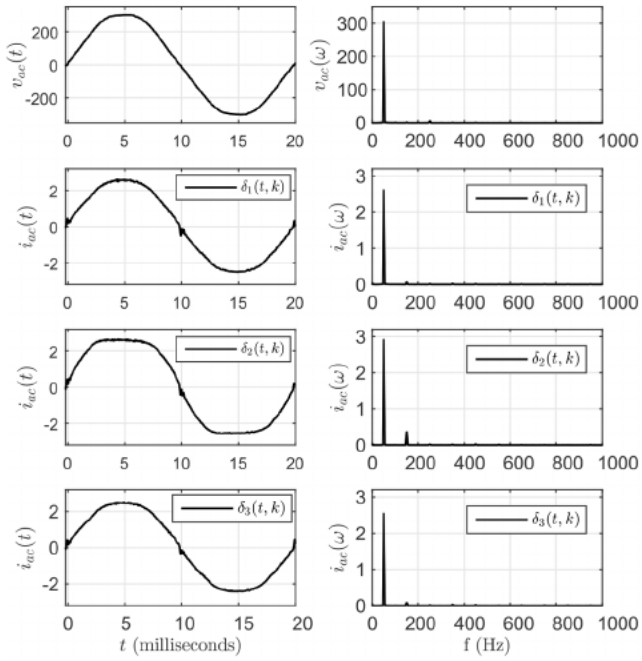

Fig. 21 *Experimental results of $v_{ac}(t)$ and $i_{ac}(t)$ in a grid period using the modulations $\delta_1(t,k)$, $\delta_2(t,k)$ and $\delta_3(t,k)$ with $k = 1$*

In Figs. 20 and 21, the power converter operation through each of the mPSM strategies used is shown for values of $k = 0.5$ and $k = 1$, respectively.

Both figures were graphically represented through the data captured from the oscilloscope and show the experimental result of $v_{ac}(t)$ and $i_{ac}(t)$ in a grid period with their corresponding frequency spectrum.

From Figs. 22–27, the experimental results obtained by means of oscilloscope screen capture show the waveforms of v_{Prim}, v_{Sec}, $v_{ac}(t)$, $i_{ac}(t)$, instantaneous power transfer defined as $P_{inst}(t)$ and digital signals to activate the switches of the AC H-bridge for each of the mPSM strategies used.

Figs. 22 and 23 correspond to the power converter operated with strategy $\delta_1(t,k)$ for k values of 0.5 and 1, respectively.

Figs. 24 and 25 correspond to the power converter operated with strategy $\delta_2(t,k)$ for k values of 0.5 and 1, respectively.

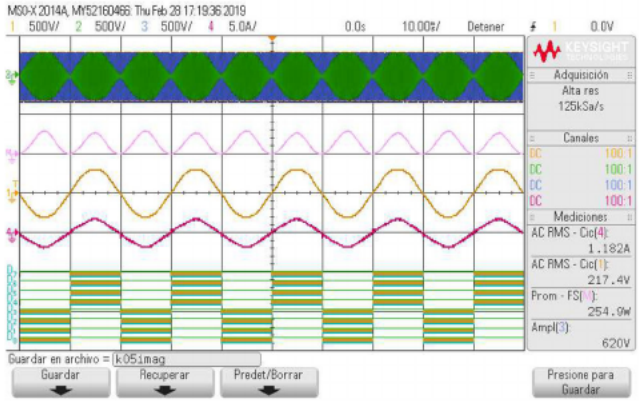

Fig. 22 *Experimental results of v_{Prim}, v_{Sec}, $P_{inst}(t)$, $v_{ac}(t)$ and $i_{ac}(t)$ and digital signal of AC H-bridge for $\delta_1(t,k)$ with $k = 0.5$*

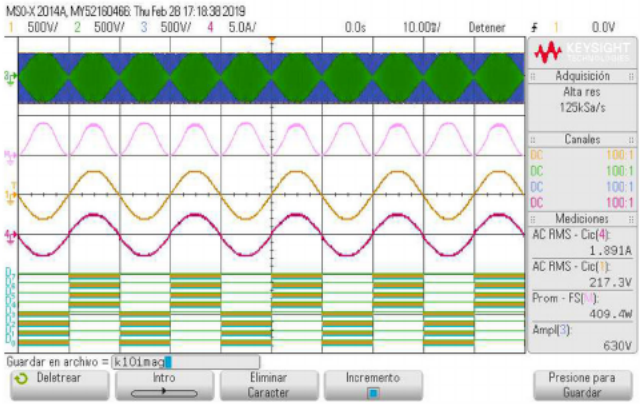

Fig. 23 *Experimental results of v_{Prim}, v_{Sec}, $P_{inst}(t)$, $v_{ac}(t)$ and $i_{ac}(t)$ and digital signal of AC H-bridge for $\delta_1(t,k)$ with $k = 1$*

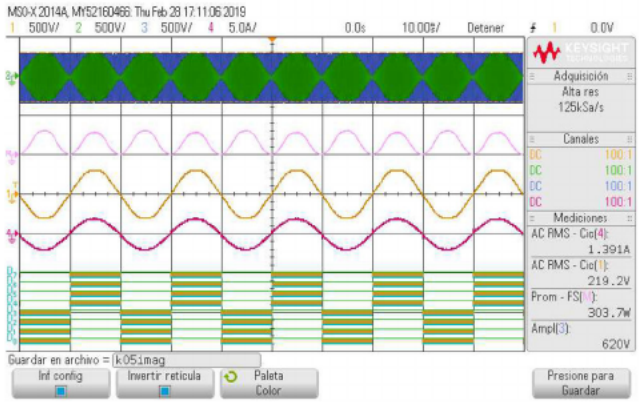

Fig. 24 *Experimental results of v_{Prim}, v_{Sec}, $P_{inst}(t)$, $v_{ac}(t)$ and $i_{ac}(t)$ and digital signal of AC H-bridge for $\delta_2(t,k)$ with $k = 0.5$*

Figs. 26 and 27 correspond to the power converter operated with strategy $\delta_3(t,k)$ for k values of 0.5 and 1, respectively.

Using the $\delta_3(t,k)$ strategy to operate the power converter, the experimental result for a change in the power flow is shown in Fig. 28.

The values of THDi and the average power transferred were calculated using k intervals every 0.1 for the three mPSM strategies applied to operate the power converter.

Normalised average power and THDi percentage are represented for the range of $|k| \leq 1$ as shown in Figs. 29 and 30, respectively.

According to the experimental results obtained, it can be observed that the waveform $i_{ac}(t)$ presents current overshoots at each cross over zero of $v_{ac}(t)$ where $nv_{Prim} = 0$. This can be deduced from the following analysis.

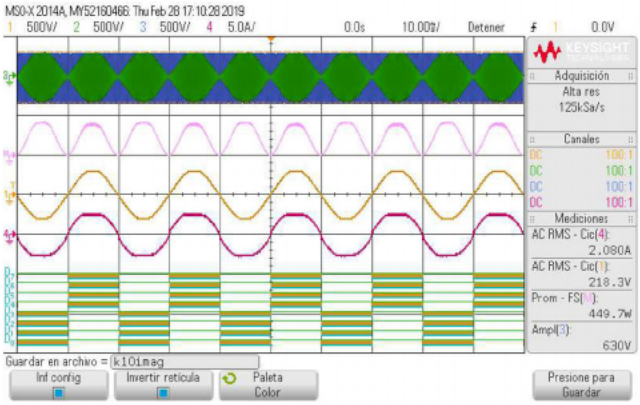

Fig. 25 *Experimental results of v_{Prim}, v_{Sec}, $P_{inst}(t)$, $v_{ac}(t)$ and $i_{ac}(t)$ and digital signal of AC H-bridge for $\delta_2(t,k)$ with $k = 1$*

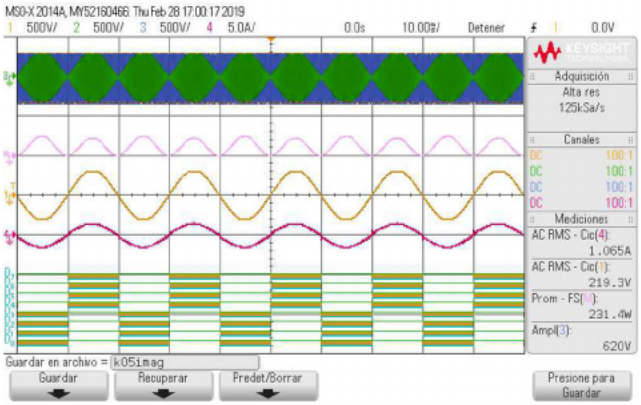

Fig. 26 *Experimental results of v_{Prim}, v_{Sec}, $P_{inst}(t)$, $v_{ac}(t)$ and $i_{ac}(t)$ and digital signal of AC H-bridge for $\delta_3(t,k)$ with $k = 0.5$*

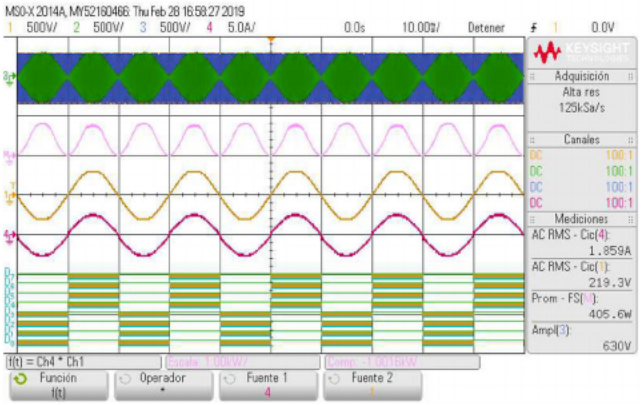

Fig. 27 *Experimental results of v_{Prim}, v_{Sec}, $P_{inst}(t)$, $v_{ac}(t)$ and $i_{ac}(t)$ and digital signal of AC H-bridge for $\delta_3(t,k)$ with $k = 1$*

At the end of each half of the grid period, the $i_{bac}(t)$ current reaches a high value as shown in Fig. 31 which can be calculated from (3).

Additionally, due to the switching strategy used, the polarity of the $i_{bac}(t)$ current changes abruptly after each cross over zero of $v_{ac}(t)$ causing an overshoots of current.

An overshoot in the $i_{bac}(t)$ current, whose value is constant, produces higher percentages of total harmonic distortion in $i_{ac}(t)$ current when the value of k is lower.

According to the calculated THDi values, it can be seen that for values of k<0.3, the experimental THDi values diverge from the theoretical values as shown in Fig. 30.

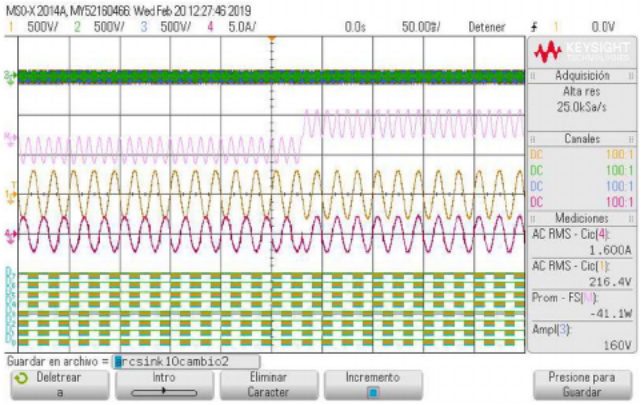

Fig. 28 *Experimental results of v_{Prim}, v_{Sec}, $P_{inst}(t)$, $v_{ac}(t)$ and $i_{ac}(t)$ and digital signal of AC H-bridge for $\delta_3(t,k)$ with power flow inversion*

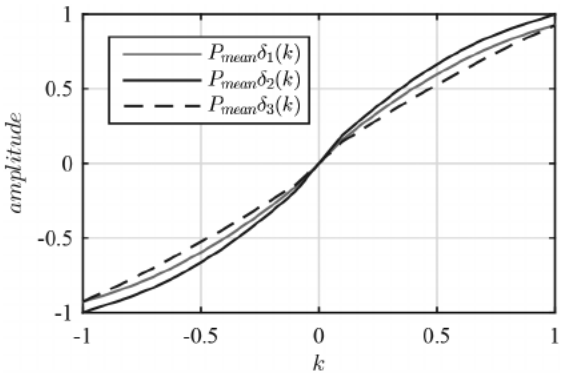

Fig. 29 *Experimental results of the normalised average power $P_{mean}\delta_1(k)$, $P_{mean}\delta_2(k)$ and $P_{mean}\delta_3(k)$ as a function of k*

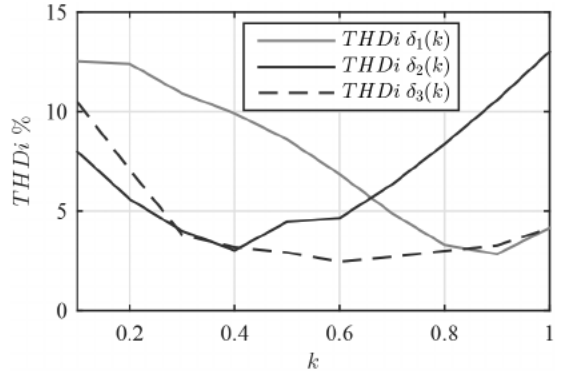

Fig. 30 *Experimental results of THDi% as a function of the factor k for each mPSM strategy used*

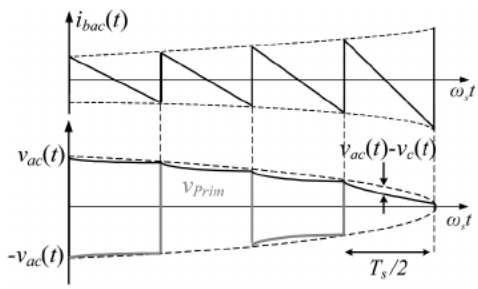

Fig. 31 *Waveform of $v_c(t)$ and $i_{bac}(t)$ a moment before zero-crossing of $v_{ac}(t)$*

4.1 Low-pass filter design

In the topology used, it can be deduced that the voltage v_{Prim} is equal to the voltage of the capacitor inverted every half period of switching.

The instantaneous voltage of the capacitor is defined as $v_c(t)$ and can be obtained by

$$v_c(t) = n\frac{1}{C_f}\int i_{bac}(t)\,\mathrm{d}t = n\frac{1}{C_f}\int i_{La}(t)\,\mathrm{d}t \tag{22}$$

where C_f is the capacitor value in μF.

Solving (22) for each $i_{La}(t)$ interval results in the following:

$$v_{c1}(t) = \frac{n}{C_f}\int_0^{\delta}\left[\frac{(nv_{\mathrm{Prim}} - v_{\mathrm{Sec}})}{L_a\omega_s}\omega_s + i_{La}(0)\right]\mathrm{d}t \tag{23}$$

$$v_{c2}(t) = \frac{n}{C_f}\int_{\delta}^{\pi}\left[\frac{(nv_{\mathrm{Prim}} - v_{\mathrm{Sec}})}{L_a\omega_s}(\omega_s - \delta) + i_{La}(\delta)\right]\mathrm{d}t \tag{24}$$

where $v_{c1}(t)$ and $v_{c2}(t)$ are the capacitor instantaneous voltages corresponding to interval 1 and 2, respectively.

According to the switching and modulation strategies used, the greatest difference between the amplitudes v_{Sec} and nv_{Prim} occurs at the zero crossings of $v_{\mathrm{ac}}(t)$.

In this case, the amplitude of v_{Prim} and the phase angle between v_{Sec} and nv_{Prim} are close to zero; thus, the instantaneous current exchange rate $\mathrm{d}i_{\mathrm{bac}}(t)/\mathrm{d}t$ reaches its maximum value.

The operating condition of the capacitor for the previous case can be considered the worst.

The waveforms of $i_{bac}(t)$ and $v_c(t)$ for the worst operating condition are shown in Fig. 31.

Depending on the system parameters defined above, the waveforms $v_c(t)$ and $v_{ac}(t)$ are not similar if the C_f value is not carefully selected.

On the other hand, to prevent the $v_c(t)$ waveform from crossing the zero-voltage axis, the difference between $v_c(t)$ and $v_{ac}(t)$ can be considered to be <10% of V_{ac} value.

Taking into account the previous consideration, the C_f value can be obtained by solving (23) for the worst operating condition as

$$C_f = \frac{n}{0.1V_{\mathrm{ac}}}\left[\frac{-v_{\mathrm{Sec}}}{L_a}\left(\frac{T_s^2}{8}\right) + \frac{v_{\mathrm{Sec}}\pi}{2L_a\omega_s}\left(\frac{T_s}{4}\right)\right] + v_c(0) \tag{25}$$

where $v_c(0)$ is the initial voltage of the capacitor.

The low-pass filter inductance defined as L_{f} can be calculated by means of (26) taking into account the C_{f} value and the cutoff frequency of the low-pass filter

$$f_c \ll f_s$$
$$L_f = \frac{1}{(2\pi f_c)^2 C_f} \tag{26}$$

where f_c is the cutoff frequency of the low-pass filter.

According to the analysis performed and considering a cutoff frequency equal to 5 kHz, the values of capacitance and inductance adopted are $C_f = 1\ \mu$F and $L_f = 1$ mH, respectively.

5 Conclusion

Three modulation strategies applied to an isolated, single-phase, single-stage, bidirectional, step-up/down AC–DC power converter for applications in electric micro-grids were analysed and compared.

The converter studied presents high-frequency harmonic components, therefore a filter is needed to attenuate them and reduce the THD*i* percentage.

A novel modulation strategy was proposed which allows to operate the power converter resulting in a phase current with low THD and PF close to 1 for the entire operating range.

In relation to the percentage of THD*i* obtained, similar theoretical and experimental results were achieved for each of the mPSM strategies applied to the power converter.

The theoretical results reached maximum percentages of THD*i* less than 12% for $\delta_1(t,k)$, 14.5% for $\delta_2(t,k)$ and 4% for $\delta_3(t,k)$.

Experimental results show a peak current in each zero crossover of $v_a(t)$ and its constant value produces higher percentages of THD*i* when the value of k is lower.

In the operation range of $0.3 < |k| \leq 1$, the experimental results achieved from the maximum percentage of THD*i* were less than 11% for $\delta_1(t,k)$, 13% for $\delta_2(t,k)$ and 5% for $\delta_3(t,k)$.

For the three mPSM strategies, theoretical and experimental PF values reached were close to 1.

With regard to the average power transfer reached for each of the mPSM strategies applied to the power converter, similar theoretical and experimental results were obtained.

Through the $\delta_1(t,k)$ and $\delta_3(t,k)$ mPSM strategies, the maximum average power transfer obtained for both cases was 382 W for the theoretical results and ∼405 W for the experimental results.

The power converter operated by the $\delta_2(t,k)$ mPSM strategy reached a maximum value of average power transferred equal to 428 W for the theoretical result and 449 W for the experimental results.

Regarding the results obtained, when operating the power converter through the $\delta_3(t,k)$ mPSM strategy, a better quality of energy is obtained at the time of the energy exchange between the micro-grid of DC and the AC grid.

6 Acknowledgments

This work was supported by the following Argentinian Agencies: Secretaría de Ciencia y Técnica de la Universidad Nacional de Río Cuarto (SeCyT, UNRC), Concejo Nacional de Investigaciones Científicas y Técnicas (CONICET), Agencia Nacional de Promoción Científica y Tecnológica (FONCyT) through the project PICT 1663/2016, and Ministerio de Ciencia y Tecnología de la Provincia de Córdoba through the project FONTEC 2018 'I + D de transformador de estado sólido para aplicaciones rurales'.

7 References

[1] Carrasco, J.M., Franquelo, L.G., Bialasiewicz, J.T., *et al.*: 'Power-electronic systems for the grid integration of renewable energy sources: a survey', *IEEE Trans. Ind. Electron.*, 2006, **53**, (4), pp. 1002–1016

[2] Liang, X.: 'Emerging power quality challenges due to integration of renewable energy sources'. 2016 IEEE Industry Applications Society Annual Meeting, Portland, OR, USA, 2016, pp. 1–9

[3] Planas, E., Andreu, J., Gárate, J.I., *et al.*: 'AC and DC technology in microgrids: a review', *Renew. Sust. Energy Rev.*, 2015, **43**, pp. 726–749

[4] Kakigano, H., Nomura, M., Ise, T.: 'Loss evaluation of DC distribution for residential houses compared with ac system'. The 2010 Int. Power Electronics Conf. – ECCE ASIA, Sapporo, Japan, 2010, pp. 480–486

[5] De Doncker, R.W.A.A., Divan, D.M., Kheraluwala, M.H.: 'A three-phase soft-switched high-power-density DC/DC converter for high-power applications', *IEEE Trans. Ind. Appl.*, 1991, **27**, (1), pp. 63–73

[6] She, X., Huang, A.Q., Burgos, R.: 'Review of solid-state transformer technologies and their application in power distribution systems', *IEEE J. Emerging Sel. Topics Power Electron.*, 2013, **1**, (3), pp. 186–198

[7] Everts, J.: 'Closed-form solution for efficient ZVS modulation of DAB converters', *IEEE Trans. Power Electron.*, 2017, **32**, (10), pp. 7561–7576

[8] Huber, J.E., Kolar, J.W.: 'Volume/weight/cost comparison of a 1 MVA 10 kV/400 V solid-state against a conventional low-frequency distribution transformer'. 2014 IEEE Energy Conversion Congress and Exposition (ECCE), Pittsburgh, PA, USA, 2014, pp. 4545–4552

[9] Moonem, M.A., Krishnaswami, H.: 'Analysis of dual active bridge based power electronic transformer as a three-phase inverter'. IECON 2012 – 38th Annual Conf. on IEEE Industrial Electronics Society, Montreal, Canada, 2012, pp. 238–243

[10] Weise, N.D., Castelino, G., Basu, K., *et al.*: 'A single-stage dual-active-bridge-based soft switched AC–DC converter with open-loop power factor correction and other advanced features', *IEEE Trans. Power Electron.*, 2014, **29**, (8), pp. 4007–4016

[11] Castelino, G., Basu, K., Mohan, N.: 'A novel three-phase bi-directional, isolated, single-stage, DAB-based AC-DC converter with open-loop power factor correction'. 2012 IEEE Int. Conf. on Power Electronics, Drives and Energy Systems (PEDES), Bangaluru, Karnataka, India, 2012, pp. 1–6

[12] Jauch, F., Biela, J.: 'Combined phase-shift and frequency modulation of a dual-active-bridge AC-DC converter with PFC', *IEEE Trans. Power Electron.*, 2016, **31**, (12), pp. 8387–8397

[13] Bosso, J.E., Oggier, G.G., García, G.O.: 'Topología de transformador de estado sólido CC-CA trifásico de una sola etapa'. 2014 IEEE Biennial Congress of Argentina (ARGENCON), Bariloche, Argentina, 2014, pp. 387–392

[14] Bosso, J., Oggier, G.G., García, G.O.: 'Evaluación de transformadores de estado sólido CC-CA'. 2014 IEEE Biennial Congress of Argentina (ARGENCON), Bariloche, Argentina, 2014, pp. 549–554
[15] Wang, M., Huang, Q., Guo, S., *et al.*: 'Soft-switched modulation techniques for an isolated bidirectional DC–AC', *IEEE Trans. Power Electron.*, 2018, **33**, (1), pp. 137–150
[16] Huber, J.E., Kolar, J.W.: 'Solid-state transformers: on the origins and evolution of key concepts', *IEEE Ind. Electron. Mag.*, 2016, **10**, (3), pp. 19–28
[17] Ebrahim Adabi, M., Martinez-Velasco, J.A.: 'Solid state transformer technologies and applications: a bibliographical survey', *AIMS Energy*, 2018, **6**, (energy-06-02-291), pp. 291–338
[18] Vangen, K., Melaa, T., Bergsmark, S., *et al.*: 'Efficient high-frequency soft-switched power converter with signal processor control'. [Proceedings] Thirteenth Int. Telecommunications Energy Conf. – INTELEC 91, Kyoto, Japan, 1991, pp. 631–639
[19] Krismer, F., Round, S., Kolar, J.W.: 'Performance optimization of a high current dual active bridge with a wide operating voltage range'. 2006 37th IEEE Power Electronics Specialists Conf., Jeju, Republic of Korea, 2006, pp. 1–7
[20] Zhou, H., Khambadkone, A.M.: 'Hybrid modulation for dual-active-bridge bidirectional converter with extended power range for ultracapacitor application', *IEEE Trans. Ind. Appl.*, 2009, **45**, (4), pp. 1434–1442
[21] Krismer, F., Kolar, J.W.: 'Closed form solution for minimum conduction loss modulation of DAB converters', *IEEE Trans. Power Electron.*, 2012, **27**, (1), pp. 174–188
[22] Wang, Y., de Haan, S.W.H., Ferreira, J.A.: 'Optimal operating ranges of three modulation methods in dual active bridge converters'. 2009 IEEE 6th Int. Power Electronics and Motion Control Conf., Wuhan, China, 2009, pp. 1397–1401
[23] Bai, H., Mi, C.: 'Eliminate reactive power and increase system efficiency of isolated bidirectional dual-active-bridge DC-DC converters using novel dual-phase-shift control', *IEEE Trans. Power Electron.*, 2008, **23**, (6), pp. 2905–2914
[24] Zhao, B., Song, Q., Liu, W.: 'Power characterization of isolated bidirectional dual-active-bridge DC-DC converter with dual-phase-shift control', *IEEE Trans. Power Electron.*, 2012, **27**, (9), pp. 4172–4176
[25] Stojadinović, M., Kalkounis, E., Jauch, F., *et al.*: 'Generalized PWM generator with transformer flux balancing for dual active bridge converter'. 2017 19th European Conf. on Power Electronics and Applications (EPE'17 ECCE Europe), Warsaw, Poland, 2017, pp. P.1–P.10
[26] Gitau, M.N., Ebersohn, G., Kettleborough, J.G.: 'Power processor for interfacing battery storage system to 725 V DC bus', *Energy Convers. Manage.*, 2007, **48**, (3), pp. 871–881
[27] Beres, R.N., Wang, X., Liserre, M., *et al.*: 'A review of passive power filters for three-phase grid-connected voltage-source converters', *IEEE J. Emerging Sel. Topics Power Electron.*, 2016, **4**, (1), pp. 54–69
[28] Llomplat, M., Bosso, J.E., Oggier, G., *et al.*: 'Comparación de topologías bidireccionales de convertidores CC-CA monofásicos'. 2017 Reunión de trabajo en Procesamiento de la Información y Control (RPIC2017), Mar del Plata, Argentina, 2017
[29] Mohan, N., Undeland, T.M., Robbins, W.P.: '*Power electronics: converters, applications and design*' (John Wiley and Sons, Inc., USA, 2003, 3rd edn.)